Segregation forces in dense granular flows: Closing the gap between single intruders and mixtures

Yifei Duan[1], Lu Jing[1], Paul B. Umbanhowar[2], Julio M. Ottino[1,2,3], and Richard M. Lueptow[1,2,3]†

[1]Department of Chemical and Biological Engineering, Northwestern University, Evanston, Illinois 60208, USA

[2]Department of Mechanical Engineering, Northwestern University, Evanston, Illinois 60208, USA

[3]Northwestern Institute on Complex Systems (NICO), Northwestern University, Evanston, Illinois 60208, USA

(Received xx; revised xx; accepted xx)

Using simulations and a virtual-spring-based approach, we measure the segregation force, F_{seg}, in size-bidisperse sphere mixtures over a range of concentrations, particle size ratios, and shear rates to develop a semi-empirical model for F_{seg} that extends its applicability from the well-studied non-interacting intruders regime to finite-concentration mixtures where cooperative phenomena occur. The model predicts the concentration below which the single intruder assumption applies and provides an accurate description of the pressure partitioning between species.

1. Introduction

Flowing granular materials segregate by particle size, density, or other physical properties, which is a phenomenon crucial to many industrial and geophysical processes (Ottino & Khakhar 2000; Ottino & Lueptow 2008; Frey & Church 2009). Despite decades of research on this topic, fundamental aspects of granular flow-driven segregation remain elusive, and state-of-the-art continuum segregation models largely rely instead on *ad hoc* or configuration-specific closure schemes (Gray 2018; Umbanhowar *et al.* 2019; Thornton 2021). Recent efforts characterizing forces on single intruder particles in otherwise species-monodisperse granular flows have advanced our understanding of segregation at the particle level (Tripathi & Khakhar 2011; Guillard *et al.* 2016; Jing *et al.* 2017; van der Vaart *et al.* 2018; Staron 2018; Jing *et al.* 2020) and led to segregation force models applicable across flow configurations (Guillard *et al.* 2016; Jing *et al.* 2021). However, it is unclear whether or how single intruder results can be applied to granular mixtures with finite species concentration (Tripathi *et al.* 2021; Rousseau *et al.* 2021). More fundamentally, the mechanisms governing changes in segregation behaviors between intruder and mixture regimes as the species concentration is varied remain unresolved.

In this paper, we extend the virtual-spring-based "force meter" approach for a single intruder particle (Guillard *et al.* 2016; van der Vaart *et al.* 2018; Jing *et al.* 2020) to size-bidisperse mixtures of arbitrary species concentration and use it to characterize the dependence of the segregation force on concentration for various particle size ratios in controlled, constant-shear-rate flow simulations, see figure 1(a). We find that the segregation force exhibits a plateau at lower concentrations and changes monotonically

† Email address for correspondence: r-lueptow@northwestern.edu

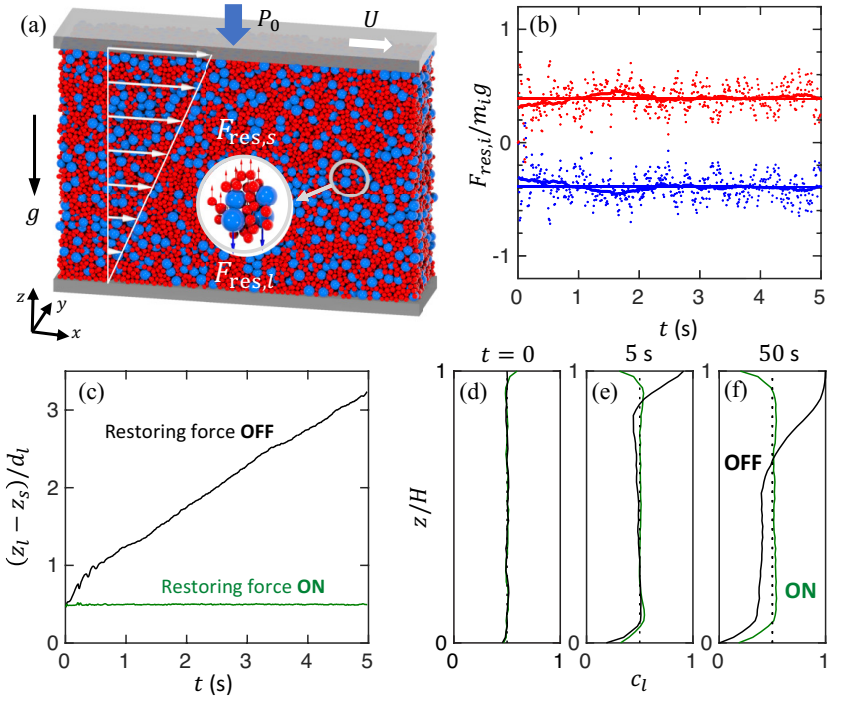

FIGURE 1. (a) Large (4 mm, blue) and small (2 mm, red) particles ($c_l = c_s = 0.5$) in a controlled, constant-shear-rate flow. (b) Scaled restoring force, $F_{\mathrm{res},i}$, vs. time for large (blue) and small (red) particles. Data points sampled at 0.01 s intervals; bold curves are averages using a 1 s long sliding window. Horizontal lines are averages from 2 s to 5 s. (c) Mean center of mass offset between species, $\bar{z}_l - \bar{z}_s$, remains unchanged from its initial value with reactive restoring forces opposing segregation. Without restoring forces, large particles rise and small particles sink, such that $\bar{z}_l - \bar{z}_s$ increases. (d-f) Local concentration of large particles away from walls (i.e., $0.1 \leqslant z/H \leqslant 0.9$) remains unchanged over time when the restoring force is ON, unlike the case without restoring forces (OFF), where the effects of segregation are clearly evident by $t = 50$ s.

above a critical concentration, indicating a transition from non-interacting intruders to cooperative phenomena in mixtures, which is reminiscent of previously observed asymmetric concentration dependence in the segregation flux (van der Vaart *et al.* 2015; Jones *et al.* 2018). We also show that these results can provide closures for connecting segregation models with continuum-based frameworks for flowing granular mixtures.

2. Simulations and methods

An in-house discrete element method (DEM) code running on CUDA-enabled NVIDIA GPUs (Isner *et al.* 2020) is used to simulate a size-bidisperse particle mixture with species volume concentration c_i, diameter d_i, and density $\rho_i = 1\,\mathrm{g/cm^3}$ ($i = l$, s for large or small particles, respectively) sheared in a streamwise (x) and spanwise (y) periodic domain of length $L = 35d_l$, width $W = 10d_l$, and height $H = 25d_l$ to $50d_l$ (varied as needed) in the presence of gravity ($g = 9.81\,\mathrm{m/s^2}$, in the negative z-direction), see figure 1(a). The standard linear spring-dashpot model (Cundall & Strack 1979) is used to resolve particle-particle and particle-wall contacts of spherical particles using a friction coefficient of 0.5, a restitution coefficient of 0.2, and a binary collision time of 0.15 ms. The contact stiffness number $\kappa = k_n/P\bar{d} \approx 10^4$ (where k_n is the normal contact stiffness, P is the local pressure, and $\bar{d} = c_l d_l + c_s d_s$ is the mean particle diameter) is sufficiently large that

particle stiffness should have negligible influence on the flow (da Cruz *et al.* 2005). We have verified that increasing or decreasing κ by an order of magnitude does not affect the simulation results. Changing bounding walls from smooth to bumpy (randomly attached particles) does not affect the results. Large ($d_l = 4\,\mathrm{mm}$) and small particles (d_s varied to adjust the size ratio, d_l/d_s) have a $\pm 10\%$ uniform size distribution to minimize layering (Staron & Phillips 2014) (increasing the size variation to $\pm 20\%$ does not alter our results). Depending on the size ratio, between 26000 and 150000 particles are included in each simulation.

A constant shear rate $\dot{\gamma} = U/H$ varied from 25 to 50 s^{-1} is imposed on the flow by the combination of the translating upper bounding wall and a streamwise stabilizing force, $F_{\mathrm{stabilize},k} = K_s(u_k - \dot{\gamma} z_k)$, on each particle k at every simulation time step, where u_k is the particle streamwise velocity, z_k is the vertical particle position, and K_s is a gain parameter (Lerner *et al.* 2012; Clark *et al.* 2018; Fry *et al.* 2018; Saitoh & Tighe 2019; Duan *et al.* 2020; Jing *et al.* 2020). This stabilizing force reduces the granular temperature in the streamwise direction but does not affect the rheological behavior (Jing *et al.* 2020) or segregation (Jing *et al.* 2021), and the constant shear rate eliminates forces associated with shear gradients (Fan & Hill 2011*a*,*b*; Guillard *et al.* 2016; Jing *et al.* 2021). An overburden pressure equal to the pressure at a depth of $H_w = 20 d_l$ (i.e., $P_{\mathrm{wall}} = \rho \phi g H_w$ where the bulk solid fraction ϕ varies from 0.56 to 0.59 depending on flow conditions) is applied using a massive flat frictional top wall that is free to move vertically (fluctuates by $\pm 2\%$ or less after an initial rapid dilation of the particles at flow onset) and moves horizontally at a velocity determined by the constant shear rate velocity profile. The inertial number, $I = \dot{\gamma} \bar{d} \sqrt{\rho/P}$, varies between 0.06 to 0.26 depending on the flow conditions, indicating a dense granular flow.

A spring-like vertical restoring force proportional to the difference in the vertical center of mass positions of the two initially mixed species is applied uniformly to all particles of each species i at every simulation time step in order to characterize the particle forces. The restoring force simultaneously suppresses segregation throughout the flow domain which otherwise would change the local species concentration. This method is inspired by the virtual-spring-based technique used in single intruder DEM simulations to measure the segregation force (Guillard *et al.* 2016; van der Vaart *et al.* 2018; Jing *et al.* 2020). The difference here is that the same virtual-spring restoring force is applied to all particles of each species rather than to just a single intruder particle, allowing us to consider a wide range of relative concentrations of the two species. This approach resembles that in a recent study where opposing forces are applied to all particles of each species to study the interspecies drag (Bancroft & Johnson 2021). Here, the restoring force on each particle of species i is $F_{\mathrm{res},i} = -K_r[(\bar{z}_i - \bar{z}_j) - (\bar{z}_{i,0} - \bar{z}_{j,0})]/N_i$, where the center of mass of species i is $\bar{z}_i = \sum_{k\in i}^{N_i} z_k V_k / \sum_{k=1}^{N} V_k$ and $\bar{z}_{i,0} = \bar{z}_i(t=0)$, V_k is the volume of particle k, subscript j indicates the other species, and N_i and N are the number of particles of species i and the total number of particles, respectively. The applied restoring forces balance, i.e.,

$$F_{\mathrm{res},i} N_i + F_{\mathrm{res},j} N_j = 0, \tag{2.1}$$

and the bulk flow behavior (e.g., shear flow, bulk pressure) is unaltered. Similar to the imposed velocity profiles, we have further confirmed both here and in previous work (Jing *et al.* 2021) that the particle restoring forces do not affect either the rheological characteristics of the flow or kinetic stress fields in the segregation direction.

Figure 1(b) plots the instantaneous restoring force scaled by particle weight, $F_{\mathrm{res},i}/m_i g$, at 0.01 s intervals for the example case shown in figure 1(a) with $d_l/d_s = 2$ and $c_l = c_s = 0.5$. The scaled restoring forces for large (blue) and small (red) particles are equal and

opposite for $c_l = c_s = 0.5$ due to the force balance, which can be written as $c_l F_{\mathrm{res},l}/m_l g + c_s F_{\mathrm{res},s}/m_s g = 0$ based on Eq. (2.1), noting that particle mass $m_i = \rho V_i$ and species volume concentration $c_i = N_i V_i / V_{\mathrm{tot}}$, where V_{tot} is the total particle volume. The time average $F_{\mathrm{res},i}/m_i g$ over 1 s time windows (bold curve) remains relatively constant 2 s after flow onset, although small force fluctuations are evident due to the stochastic nature of granular flows. In addition, varying the uniform shear rate $\dot{\gamma}$, the layer thickness H, or the gain parameters K_s and K_r have minimal influence on $F_{\mathrm{res},i}/m_i g$, indicating that the restoring force is independent of the details of the flow geometry and control parameters, and that its effect is uniform through the depth of the particle bed.

To demonstrate the effectiveness of the restoring force in balancing the segregation force, the center of mass offset between the two species scaled by the large particle diameter is shown in figure 1(c). Note that $(\bar{z}_l - \bar{z}_s)/d_l \approx 0.5$ at $t = 0$, which is close to the ideal uniformly mixed value of 0 (our dense packing is achieved by placing particles in a grid pattern and letting them settle under gravity before applying shear, which results in the slight initial offset between the centers of mass of the two species of $0.5d_l$). Without restoring forces, $(\bar{z}_l - \bar{z}_s)/d_l$ increases with time as the two species segregate with a constant segregation velocity after an initial dilation of particles ($t < 0.5$ s) following flow onset at $t = 0$. The segregation velocity remains nearly constant until the local particle concentration changes enough to affect the segregation, typically after 20 s, depending on particle properties and flow conditions. In contrast, with the restoring force ON to reactively balance the segregation force, $(\bar{z}_l - \bar{z}_s)/d_l$ remains near its initial value of 0.5, corresponding to no segregation.

The effectiveness of the restoring force in maintaining the mixed (unsegregated) state is also evident in the concentration profiles in figure 1(d-f), where c_l remains at its initial value of 0.5 away from the walls (i.e. $0.1 \leqslant z/H \leqslant 0.9$) when the restoring force is ON. Near the walls c_l slightly decreases, because small particles can reside closer to the walls than the large particles. This wall exclusion effect due to particle size differences does not change the mean center of mass offset between species, $\bar{z}_l - \bar{z}_s$. As a result, the force measurement approach is unaffected. For example, doubling the layer thickness H significantly decreases the proportion of the flow affected by the walls, but the measured segregation force differs by less than 5%. With the restoring forces OFF, segregation occurs throughout the depth of the layer with a local segregation rate inversely proportional to the square root of depth (Duan *et al.* 2020). As a result, c_l deviates from 0.5 with noticeable segregation near the top wall ($z/H > 0.7$) at $t = 5$ s (figure 1e) and throughout the layer at $t = 50$ s (figure 1f).

Since $F_{\mathrm{res},i}$, which is determined as the time-average of the reactive restoring force, balances the particle segregation force, $F_{\mathrm{seg},i}$ and the particle weight, $m_i g$,

$$F_{\mathrm{seg},i} = m_i g - F_{\mathrm{res},i}. \tag{2.2}$$

$F_{\mathrm{seg},i}$ is always upward, opposing gravity. Since $F_{\mathrm{res},s} > 0$ (figure 1b), $F_{\mathrm{seg},s} < m_s g$ so small particles would sink without the restoring force; likewise, since $F_{\mathrm{res},l} < 0$, $F_{\mathrm{seg},l} > m_l g$ so large particles would rise without the restoring force. From here on, we scale the segregation force with the particle weight, $\hat{F}_i = F_{\mathrm{seg},i}/m_i g$.

3. Results

The first key result of this paper is measurements of the dependence of the segregation force on concentration for various particle size ratios. Figure 2(a-c) shows examples of the dimensionless segregation force, $\hat{F}_i$ (symbols) vs. concentration for three size ratios ($d_l/d_s = 1.3$, 2, and 3), where the error bars reflect fluctuations of the reactive restoring

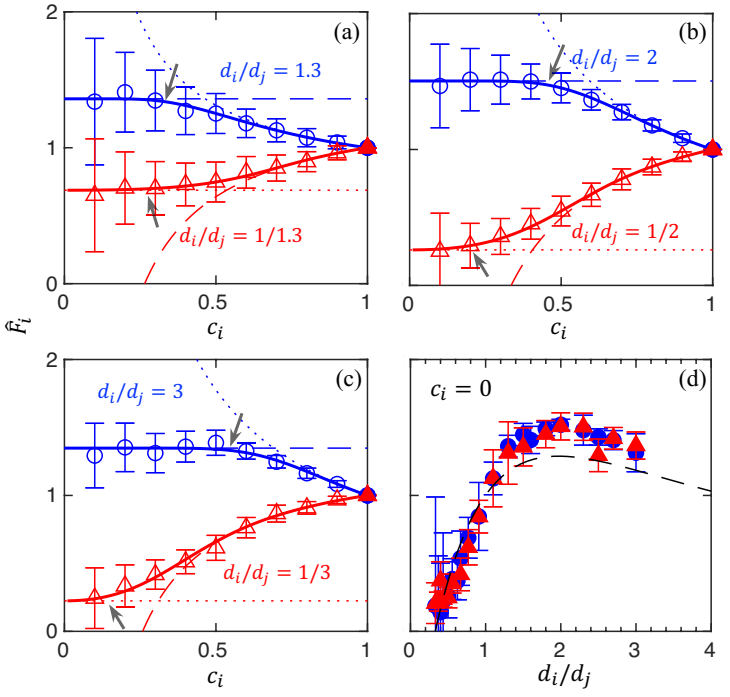

FIGURE 2. (a-c) Scaled particle segregation force $\hat{F}_i = F_{\mathrm{seg},i}/m_i g$ vs. species concentration c_i for large (○) and small (△) particles with size ratio d_l/d_s=1.3 (a), 2 (b), and 3 (c). Error bars are the standard deviation for the time-average of $F_{\mathrm{res},i}$. Dashed and dotted curves are predictions of the single intruder segregation force model extended to mixtures [Eq. (3.2)]. Solid curves are fits of Eq. (3.3) using large particle data. Arrows indicate the concentration $c_{i,\mathrm{crit}}$ where F_i deviates from the intruder limit, see text. (d) $\hat{F}_{i,0}$ from fits of Eq. (3.3) to large (●) and small (▲) particle data. Dashed curve is a single intruder model based on single intruder simulations (Jing *et al.* 2020).

force in figure 1(b). Although the error bars are relatively large at low concentrations, $\hat{F}_i$ clearly plateaus to a maximal (minimal) value approaching the single intruder limit $\hat{F}_{i,0}$ at $c_i \approx 0$ and decreases (increases) monotonically with c_i for large (small) particles. For both small and large species, $\hat{F}_{i,1} = 1$ (or, equivalently, $F_{\mathrm{seg},i} = m_i g$) in the monodisperse limit ($c_i = 1$), since the segregation force exactly offsets the particle weight.

Details of the dependence of $\hat{F}_i$ on c_i vary with the size ratio, d_i/d_j. First, consider figure 2(a) for $d_l/d_s = 1.3$ (corresponding to $d_i/d_j = 1.3$ and 1/1.3), which shows that the plateau in $\hat{F}_i$ for both species extends from $c_i = 0$ to a critical concentration, $c_{i,\mathrm{crit}} \approx 0.3$ (defined precisely below). For $c_i < c_{i,\mathrm{crit}}$, particles of species i interact so infrequently with each other that the segregation force acting on them is essentially that for a single intruder particle (i.e., concentration independent). As c_i increases beyond $c_{i,\mathrm{crit}}$, interactions between particles of species i become significant, eventually resulting in the segregation force approaching the monodisperse limit as c_i approaches one. The segregation force plateau extends to higher concentrations (greater than 0.5) as d_i/d_j increases, see figure 2(b,c). Furthermore, $c_{l,\mathrm{crit}} \geqslant c_{s,\mathrm{crit}}$, indicating that large particles act like intruders at higher concentrations than small particles. For example, for $d_l/d_s = 3$ (figure 2c) the plateau for large particles extends to $c_{l,\mathrm{crit}} \approx 0.6$, which is nearly four times the value of $c_{s,\mathrm{crit}} \approx 0.15$. Results similar to those in figures 2(a-c) are obtained for seven additional size ratios in the range $1 < d_l/d_s \leqslant 3$ considered here.

The total segregation force across both species for the entire system, which sums to the total particle weight, can be expressed using Eqs. (2.1) and (2.2), as

$$\hat{F}_i c_i + \hat{F}_j c_j = 1. \tag{3.1}$$

Noting that $c_j = 1 - c_i$ and $\hat{F}_j = F_{j,0}$ for $c_j \leqslant c_{j,\mathrm{crit}}$ (or, equivalently, $c_i \geqslant 1 - c_{j,\mathrm{crit}}$), we can predict $\hat{F}_i$ for mixtures not only in the intruder regime of species i, but also in the intruder regime of species j,

$$\hat{F}_i = \begin{cases} \hat{F}_{i,0} & c_i \leqslant c_{i,\mathrm{crit}}, \\ \left[1 - \hat{F}_{j,0}(1 - c_i)\right]/c_i & c_i \geqslant 1 - c_{j,\mathrm{crit}}. \end{cases} \tag{3.2}$$

Figures 2(a-c) show that the predictions of Eq. (3.2) for both large (dashed curves) and small particles (dotted curves) match the segregation force data (symbols) in the vicinity of the concentration extremes when $\hat{F}_{i,0}$ and $\hat{F}_{j,0}$ are based on the intruder-limit values given in figure 2(d) and determined by fitting the data to Eq. (3.3) as described shortly. That is, determining $\hat{F}_{l,0}$ for $c_l < c_{l,\mathrm{crit}}$ for large particles (dashed blue horizontal line) leads to the corresponding prediction for $\hat{F}_s$ at large c_l (dashed red curve) and likewise for small particles (dotted red horizontal line and dotted blue curve). This approximation fits the data well, except in the middle of the concentration range where the initial deviation of the data from the horizontal line reflects the approximate value of $c_{i,\mathrm{crit}}$.

Though Eq. (3.2) combined with $\hat{F}_{i,0}$ and $\hat{F}_{j,0}$ predict $\hat{F}_i$ at the concentration extremes, a greater challenge is to model $\hat{F}_i$ in the intermediate transition regime (i.e., $c_{i,\mathrm{crit}} < c_i < 1 - c_{j,\mathrm{crit}}$). Since $\hat{F}_i$ is bounded at both ends of the concentration range, we propose a relation of the form

$$\hat{F}_l = 1 + (\hat{F}_{l,0} - 1)\tanh\left(\frac{1 - \hat{F}_{s,0}}{\hat{F}_{l,0} - 1}\frac{c_s}{c_l}\right) \tag{3.3a}$$

for large particles, noting that the characteristics of the hyperbolic tangent function, i.e. $\lim_{c_l \to 0}\tanh(c_s/c_l) = 1$ and $\lim_{c_l \to 1}\tanh(c_s/c_l) = 0$, satisfy the theoretical constraints that $\hat{F}_l = \hat{F}_{l,0}$ at $c_l = 0$ and $\hat{F}_l = 1$ at $c_l = 1$. Substituting Eq. (3.3a) into the force balance of Eq. (3.1) and solving for $\hat{F}_s$ gives

$$\hat{F}_s = 1 - (\hat{F}_{l,0} - 1)\frac{c_l}{c_s}\tanh\left(\frac{1 - \hat{F}_{s,0}}{\hat{F}_{l,0} - 1}\frac{c_s}{c_l}\right). \tag{3.3b}$$

Equation (3.3b) also satisfies the same constraints at both concentration limits, i.e. $\hat{F}_s = \hat{F}_{s,0}$ at $c_s = 0$ and $\hat{F}_s = 1$ at $c_s = 1$. $\hat{F}_{l,0}$ and $\hat{F}_{s,0}$ correspond to intruder segregation forces and can be obtained by fitting Eq. (3.3a) to the data for large particles or, equivalently, fitting Eq. (3.3b) to the data for small particles with no significant differences in the fit quality or fit parameter values.

To demonstrate the validity of our simulation and fitting approach, figure 2(d) shows $\hat{F}_{i,0}$ based on curve fits to Eq. (3.3) for both large (blue circles) and small (red triangles) particle data. The two data sets match within the uncertainty, demonstrating the robust nature of the hyperbolic functional form of Eq. (3.3) in characterizing the segregation force. In addition, the results are comparable to predictions (dashed curve) of a single intruder model derived from single intruder simulations (Jing *et al.* 2020), even though these simulations use different particle properties (i.e., $d_l = 1 - 40\,\mathrm{mm}$, $d_s = 5\,\mathrm{mm}$, and $\rho = 2.5\,\mathrm{g/mm^3}$), implement a different contact model (i.e., Hertz contact model with Young's modulus of $5{\times}10^7\,\mathrm{Pa}$ and Poison's ratio 0.4), use a different flow geometry (inclined chute and uniform shear), and have a slightly lower solid volume fraction ($\phi = 0.55$ instead of $\phi = 0.56 - 0.59$ here). This validates not only the values we find

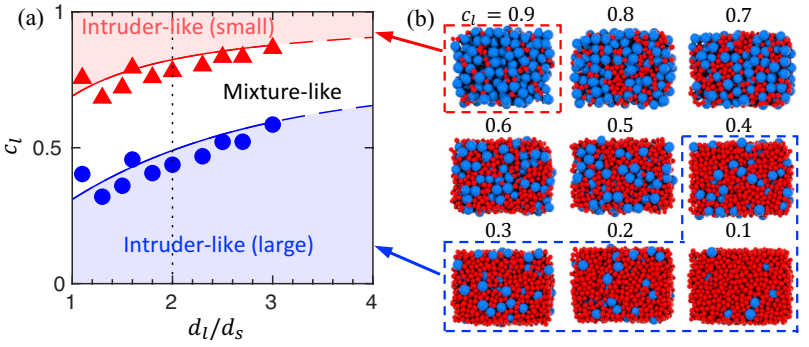

FIGURE 3. (a) Segregation force regimes (shaded areas) dependence on large particle concentration, c_l, and size ratio, d_l/d_s. Symbols represent $c_{i,\mathrm{crit}}$ for large (●) and small (▲) particles. Curves are $c_{i,\mathrm{crit}} = 0.74[1 - \exp(-0.52 d_i/d_j)]$ (see text). (b) Sheared bed images for $d_l/d_s = 2$ [vertical dotted line in (a)] at c_l intervals of 0.1. For $c_s < c_{s,\mathrm{crit}} \approx 0.18$ (or, equivalently, $c_l \gtrapprox 0.82$) the small particle segregation force equals that on a single small intruder, while for $c_l < c_{l,\mathrm{crit}} \approx 0.46$ the large particle segregation force equals that on a single large intruder. Intermediate concentrations ($0.46 \lessapprox c_l \lessapprox 0.82$), where segregation forces are less than for intruders, are termed mixture-like.

for the segregation force at the single intruder limit, but also our approach for direct measurement of segregation forces in bidisperse mixtures.

With an accurate model for $\hat{F}_i$, i.e. Eq. (3.3), we now define the critical concentration, $c_{i,\mathrm{crit}}$, as the concentration at which $\hat{F}_i - 1$ deviates by 5% from $\hat{F}_{i,0} - 1$. Based on 260 simulations at different concentrations, size ratios, and shear rates, and fitting the resulting segregation force data to Eq. (3.3), the dependence of $c_{i,\mathrm{crit}}$ for a wide range of conditions can be determined. The phase diagram in figure 3(a) shows the dependence of $c_{i,\mathrm{crit}}$, which describes the limiting concentration below which a particle acts as an intruder and above which cooperative phenomena between similar particles makes the system act like a mixture. This is the second key result of this paper.

In figure 3(a), $c_{i,\mathrm{crit}}$ (symbols) for both large and small particles increases monotonically with size ratio for the range explored here ($1 < d_l/d_s \leqslant 3$) and is reasonably well fit by the expression $c_{i,\mathrm{crit}} = 0.74[1 - \exp(-0.52 d_i/d_j)]$. The limiting value of $c_{i,\mathrm{crit}} = 0.74$ for $d_i/d_j \gg 1$ matches the free sifting limit for small particles in a network of randomly close-packed large particles at $\phi_{\max} = 0.64$, i.e., $1/(2 - \phi_{\max})$ (Prasad *et al.* 2017). This suggests that for $c_l > 0.74$ small particles percolate downward through the voids without significantly affecting the flow of large particles, indicating a possible change in the size segregation mechanism (Golick & Daniels 2009; Schlick *et al.* 2015).

In the monodisperse mixture limit ($d_i/d_j = 1$), the exponential fit gives $c_{i,\mathrm{crit}} = 0.30$, which implies that the corresponding large particle concentration for $c_{s,\mathrm{crit}}$ is $c_l = 1 - c_{s,\mathrm{crit}} = 0.70$, as shown in figure 3(a). Values of c_l for $c_{l,\mathrm{crit}}$ and $c_{s,\mathrm{crit}}$ are necessarily symmetric about $c_l = 0.5$, since the intruder is the same as the surrounding particles. Intriguingly, $c_{i,\mathrm{crit}} = 0.30$ is nearly identical to 0.31, the conducting sphere concentration at which disordered packings of monodisperse conducting and insulating spheres become globally conductive (i.e., exhibit long range electrical conduction, thereby exceeding what is known as the "percolation threshold") (Powell 1979; Ziff & Torquato 2017). Further, the critical concentrations for $1/3 \leqslant d_s/d_l < 1$ from this study also match the percolation thresholds in size-bidisperse mixtures (He & Ekere 2004), suggesting that the particle segregation force and geometric percolation are related. Anecdotal support for this picture is provided by figure 3(b), which shows shear flow images for

$d_l/d_s = 2$. In the intruder-like regime for small particles (large c_l), small particles appear to contact each other infrequently and only in the voids between large particles, whereas in the intruder-like regime for large particles (small c_l), large particles appear to be well-separated by a continuous phase of small particles on average, and are therefore unlikely to interact directly with each other. In an attempt to better understand the connection between the intruder regimes and the percolation limit, the coordination number and the radial distribution function of each species were evaluated for mixtures with different size ratios. However, unlike the segregation force, these quantities vary smoothly over the concentration range, failing to duplicate the plateau and rapid change in $F_{\mathrm{seg},i}$ near $c_{i,\mathrm{crit}}$ (see Appendix A). Further investigation of the intruder regime transition at $c_{i,\mathrm{crit}}$ is clearly necessary but is beyond the scope of this paper.

4. Discussion and conclusions

Our results characterizing the segregation force can be applied to continuum descriptions of segregation. Some previous studies assume $\hat{F}_i$ depends linearly on c_i to close the momentum equation (Gray & Thornton 2005; Rousseau *et al.* 2021). Despite some success for these continuum models in predicting concentration profiles of equal-volume mixtures, a linear relation between $\hat{F}_i$ and c_i does not capture the segregation force plateau for intruders clearly evident in figure 2(a-c). In addition, the resulting symmetric form for the species-specific pressure, when coupled with a linear drag model, does not predict the asymmetric concentration dependence of segregation (i.e., small particles among mostly large particles segregate faster than *vice versa*) (Golick & Daniels 2009; Gajjar & Gray 2014; Jones *et al.* 2018). To address the asymmetric segregation flux, $\hat{F}_i$ has been proposed to be quadratic in c_i (Gajjar & Gray 2014; Tripathi *et al.* 2021; Duan *et al.* 2021; Trewhela *et al.* 2021). Although the coefficients in a quadratic model can be adjusted to minimize the difference between the model and the data, the quadratic form cannot reproduce the plateau approaching the intruder limit ($c_i \approx 0$), as will be shown shortly.

To address these shortcomings in modeling the segregation force within a continuum model framework, we recast our results (data and model [Eq. (3.3)]) as partial pressures (normal stresses), i.e., $\partial P_i/\partial z = N_i F_{\mathrm{seg},i}/LWH = n_i F_{\mathrm{seg},i}$ (Rousseau *et al.* 2021), where $n_i = c_i\phi/V_i$ is the particle number density. Combined with the bulk pressure gradient $\partial P/\partial z = \phi\rho g$, the ratio of the pressure contribution of species i to the bulk pressure, or normal stress fraction, is $f_i = P_i/P = c_i\hat{F}_i$ (Tunuguntla *et al.* 2017), which, unlike the standard mixture theory, does not necessarily equal the species volume fraction.

Having measured $\hat{F}_i$ vs. c_i, we can directly evaluate f_i as figure 4(a-c) shows for three examples at $d_l/d_s = 1.3$, 2, and 3. At all concentrations, the pressure partition functions for large and small particles sum to 1 (i.e., $f_l + f_s = 1$), and the curves based on the segregation force model of Eq. (3.3) match the simulation data. The deviation of the pressure partitioning for $d_l/d_s \neq 1$ from the linear monodisperse case, $f_i = c_i$ (dotted line) is evident. Two previously proposed models assuming f_i is a weighted function of particle size, $f_i = d_i c_i / \sum d_i c_i$ (Marks *et al.* 2012), or volume, $f_i = d_i^3 c_i / \sum d_i^3 c_i$ (Tunuguntla *et al.* 2014) have been shown (Tunuguntla *et al.* 2017) to be significantly less accurate than the quadratic model of Gajjar and Gray (2014) for the partial kinetic stress for $1.3 \leqslant d_l/d_s \leqslant 1.7$ in a free surface flow, but the results for the normal stress are inconclusive. Basing the normal stress fraction f_i on the particle size (Marks *et al.* 2012) or volume (Tunuguntla *et al.* 2014) does not match our uniform shear flow data over the range of $1.1 \leqslant d_l/d_s \leqslant 3$ (see Appendix B). The Gajjar and Gray (2014) model, which is included in figure 4(a-c), can be made to match the f_i data by fitting two arbitrary model

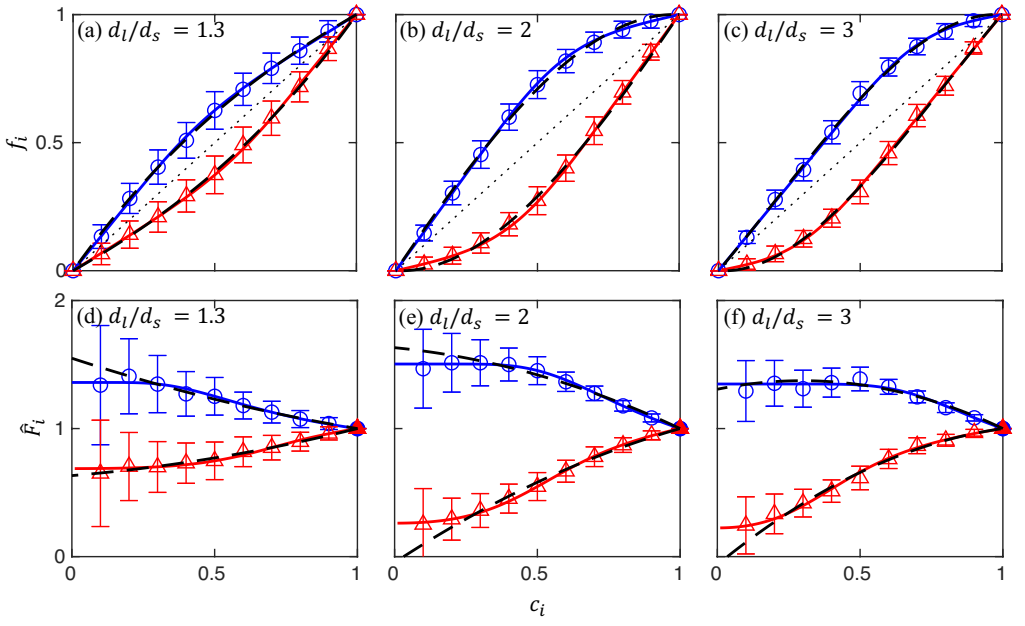

FIGURE 4. (a-c) Ratio of species specific pressure to bulk pressure, $f_i = P_i/P$, for different size ratios. Symbols represent data for large (○) and small (△) particles. Solid curves are predictions of Eq. (3.3) recast as a pressure ratio, i.e., $f_i = c_i\hat{F}_i$. Dashed black curves are best fits of the quadratic Gajjar and Gray (2014) model to the data for each size ratio, d_l/d_s. Dotted lines represent the monodisperse case ($d_l/d_s = 1$) where $f_i = c_i$. (d-f) Scaled segregation force from simulation data (symbols), $\hat{F}_i = f_i/c_i$, is well fit over the full c_i range by Eq. (3.3) (solid curves) but poorly fit by the quadratic model (black dashed curves) at low c_i. Data and Eq. (3.3) fits are reproduced from Fig. 2(a-c).

parameters via a least squares approach. However, when compared to measurements of $\hat{F}_i$ in figure 4(d-f), it is evident that Eq. (3.3) better captures the intruder plateau as c_i approaches zero. We further note that the fit parameters for the Gajjar and Gray (2014) model are not universal, depend on d_l/d_s, and lack a physical meaning, whereas Eq. (3.3) depends only on the physically meaningful and measurable single-intruder limit segregation forces, $\hat{F}_{l,0}$ and $\hat{F}_{s,0}$. Thus, the pressure partition function based on Eq. (3.3), i.e. $f_i = c_i\hat{F}_i$ where $\hat{F}_i$ is determined from Eq. (3.3), shows promise for application to continuum models of flowing mixtures of bidisperse granular materials (Marks *et al.* 2012; Tunuguntla *et al.* 2014; Staron & Phillips 2015; Tripathi *et al.* 2021; Rousseau *et al.* 2021; Trewhela *et al.* 2021), although further work is necessary to elucidate any differences between the uniform shear flow studied here and more general free surface flows.

Our results capture and characterize the concentration dependence of the segregation force in uniform shear flows, but a word of caution about extensions is in order. Recent studies indicate that the intruder segregation force $\hat{F}_{i,0}$ also depends on the shear gradient (Fan & Hill 2011*a*,*b*; Guillard *et al.* 2016; Jing *et al.* 2021). Although the shear rate gradient-induced component of F_{seg} is negligible in most free surface flows (Jing *et al.* 2020), further study of the concentration dependence of F_{seg} in flows where shear rate gradients matter (e.g., wall driven flows) and for larger size ratios, where free sifting of small particles alters the segregation, is warranted.

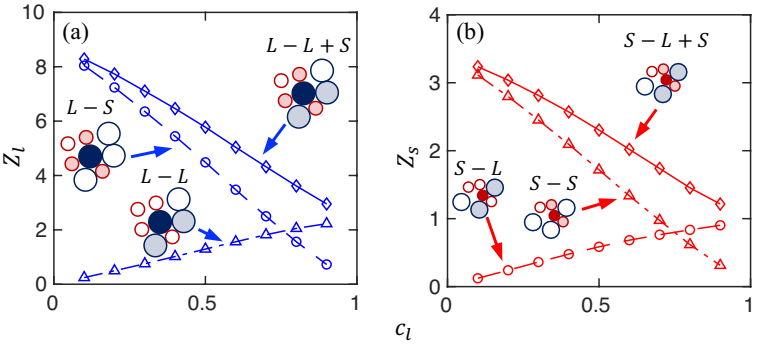

FIGURE 5. Dependence of coordination number Z_i for (a) large and (b) small particles on large particle concentration for size ratio $d_l/d_s = 2$. Z_i for large or small particles (solid curve) can be separated into sames-species (dash-dot) and inter-species (dashed) coordination numbers depending on the species of the contacting particles.

Acknowledgements

This material is based upon work supported by the National Science Foundation under Grant No. CBET-1929265.

Declaration of interests

The authors report no conflict of interest.

Appendix A. Coordination number and radial distribution function

To explore the difference in local structure between intruder and mixture regimes, the coordination number Z_i is plotted as a function of large particle concentration c_l for an example case with size ratio $d_l/d_s = 2$ in figure 5. Unlike the segregation force, Z_i for both large and small particles varies nearly linearly over the concentration range, failing to duplicate the plateau and change in segregation force near $c_{l,\mathrm{crit}} \approx 0.46$ for size ratio 2. Likewise, Z_i for different types of particle interactions is nearly linear in c_l, with no indication of abrupt changes in contact behaviour between the intruder and mixture regimes.

The radial distribution function (RDF), $g(r)$, of large and small particles neighbouring large particles at the center of the domain are plotted in figure 6. Here large particles are chosen as reference points because the segregation force plateau extends to higher concentration. For the example case with $d_l/d_s = 2$, the RDF for both large and small particles at $c_l = 0.4$, 0.5, and 0.6 are almost the same, also indicating no significant changes in the local structure of neighbouring particles near $c_{l,\mathrm{crit}} \approx 0.46$ for $d_l/d_s = 2$.

Appendix B. Other models for f_i

Previously proposed models assume that f_i is a weighted function of particle size, $f_i = d_i c_i / \sum d_i c_i$ (Marks *et al.* 2012), or volume, $f_i = d_i^3 c_i / \sum d_i^3 c_i$ (Tunuguntla *et al.* 2014). These approaches do not fit our simulation data for f_i [figure 7(a-c)] or $\hat{F}_i$ [figure 7(d-f)] in uniform shear flows.

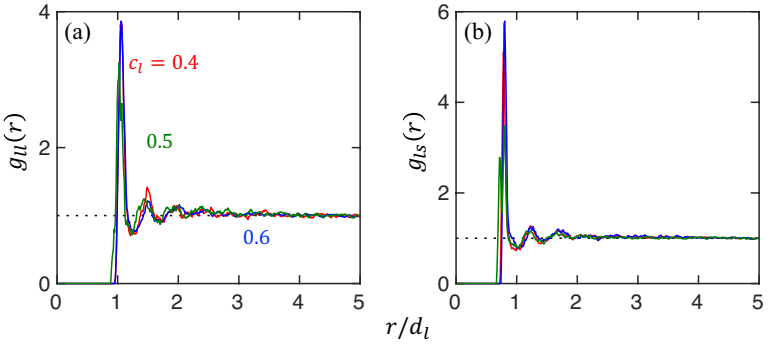

FIGURE 6. Radial distribution functions of (a) large and (b) small particles near $c_{l,\mathrm{crit}} \approx 0.5$ for $d_l/d_s = 2$. Large particles at the center of the domain are used as reference points. Data are averaged over 200 distinct times at intervals of 0.01 s. Colors represent different mixture concentrations as indicated in (a).

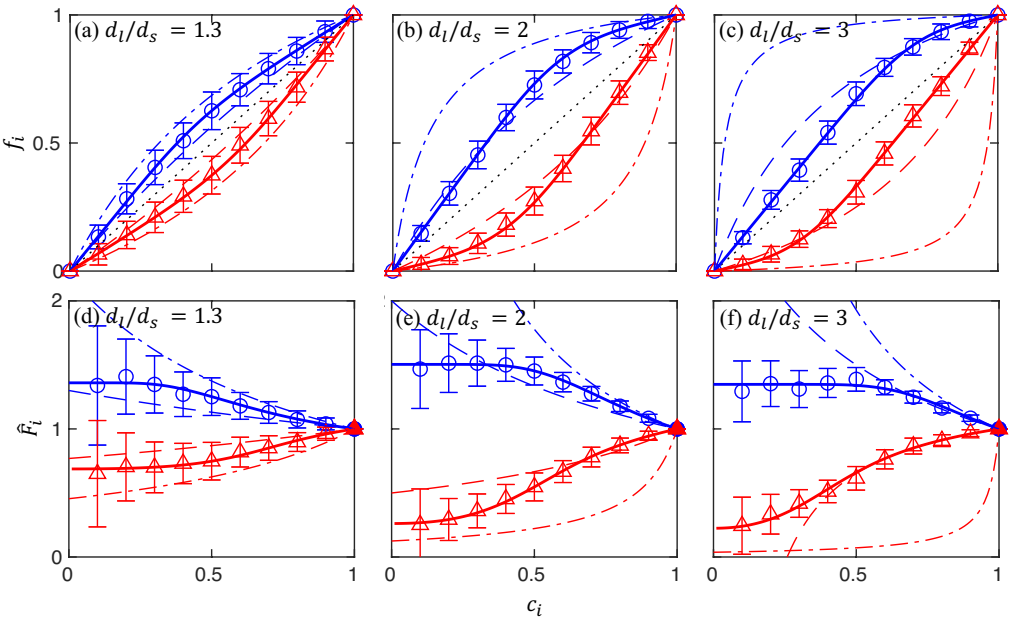

FIGURE 7. (a-c) Ratio of species specific pressure to bulk pressure, $f_i = P_i/P$, for different size ratios. Symbols represent data for large (○) and small (△) particles. Solid curves are predictions of Eq. (3.3) recast as a pressure ratio, i.e., $f_i = c_i\hat{F}_i$. Thin curves are f_i as assumed in previous studies: $f_i = d_ic_i/\sum d_ic_i$ (dashed) (Marks *et al.* 2012) and $f_i = d_i^3c_i/\sum d_i^3c_i$ (dash-dot) (Tunuguntla *et al.* 2014). Dotted lines represent the monodisperse case ($d_l/d_s = 1$) where $f_i = c_i$. (d-f) The dependence of the scaled segregation force, $\hat{F}_i = f_i/c_i$, on c_i for various models compared to simulation data and Eq. (3.3). Data and Eq. (3.3) fits are reproduced from Fig. 2(a-c).

REFERENCES

Bancroft, R. S. J. & Johnson, C. G. 2021 Drag, diffusion and segregation in inertial granular flows. *J. Fluid Mech.* **924**.

Clark, A. H., Thompson, J. D., Shattuck, M. D., Ouellette, N. T. & O'Hern, C. S. 2018 Critical scaling near the yielding transition in granular media. *Phys. Rev. E* **97** (6), 062901.

da Cruz, F., Emam, S., Prochnow, M., Roux, J.-N. & Chevoir, F. 2005 Rheophysics of dense granular materials: Discrete simulation of plane shear flows. *Phys. Rev. E* **72** (2), 021309.

Cundall, P. A. & Strack, O. D. L. 1979 A discrete numerical model for granular assemblies. *Géotechnique* **29** (1), 47–65.

Duan, Y., Umbanhowar, P. B., Ottino, J. M. & Lueptow, R. M. 2020 Segregation models for density-bidisperse granular flows. *Phys. Rev. Fluids* **5**, 044301.

Duan, Y., Umbanhowar, P. B., Ottino, J. M. & Lueptow, R. M. 2021 Modelling segregation of bidisperse granular mixtures varying simultaneously in size and density for free surface flows. *J. Fluid Mech.* **918**, A20.

Fan, Y. & Hill, K. M. 2011*a* Phase transitions in shear-induced segregation of granular materials. *Phys. Rev. Lett.* **106** (21), 218301.

Fan, Y. & Hill, K. M. 2011*b* Theory for shear-induced segregation of dense granular mixtures. *New J. Phys.* **13** (9), 095009.

Frey, P. & Church, M. 2009 How river beds move. *Science* **325** (5947), 1509–1510.

Fry, A. M., Umbanhowar, P. B., Ottino, J. M. & Lueptow, R. M. 2018 Effect of pressure on segregation in granular shear flows. *Phys. Rev. E* **97**, 062906.

Gajjar, P. & Gray, J. M. N. T. 2014 Asymmetric flux models for particle-size segregation in granular avalanches. *J. Fluid Mech.* **757**, 297–329.

Golick, L. A. & Daniels, K. E. 2009 Mixing and segregation rates in sheared granular materials. *Phys. Rev. E* **80**, 042301.

Gray, J. M. N. T. 2018 Particle segregation in dense granular flows. *Annu. Rev. Fluid Mech.* **50**, 407–433.

Gray, J. M. N. T. & Thornton, A. R. 2005 A theory for particle size segregation in shallow granular free-surface flows. *Proc. R. Soc. A* **461** (2057), 1447–1473.

Guillard, F., Forterre, Y. & Pouliquen, O. 2016 Scaling laws for segregation forces in dense sheared granular flows. *J. Fluid Mech.* **807**, R1.

He, D. & Ekere, N. N. 2004 Effect of particle size ratio on the conducting percolation threshold of granular conductive–insulating composites. *J. Phys. D* **37** (13), 1848.

Isner, A. B., Umbanhowar, P. B., Ottino, J. M. & Lueptow, R. M. 2020 Axisymmetric granular flow on a bounded conical heap: Kinematics and size segregation. *Chem. Eng. Sci.* **217**, 115505.

Jing, L., Kwok, C. Y. & Leung, Y. F. 2017 Micromechanical origin of particle size segregation. *Phys. Rev. Lett.* **118** (11), 118001.

Jing, L., Ottino, J. M., Lueptow, R. M. & Umbanhowar, P. B. 2020 Rising and sinking intruders in dense granular flows. *Phys. Rev. Res.* **2** (2), 022069.

Jing, L., Ottino, J. M., Lueptow, R. M. & Umbanhowar, P. B. 2021 A unified description of gravity-and kinematics-induced segregation forces in dense granular flows. *J. Fluid Mech.* **925**, A29.

Jones, R. P., Isner, A. B., Xiao, H., Ottino, J. M., Umbanhowar, P. B. & Lueptow, R. M. 2018 Asymmetric concentration dependence of segregation fluxes in granular flows. *Phys. Rev. Fluids* **3**, 094304.

Lerner, Edan, Düring, Gustavo & Wyart, Matthieu 2012 A unified framework for non-Brownian suspension flows and soft amorphous solids. *Proc. Natl. Acad. Sci.* **109** (13), 4798–4803.

Marks, B., Rognon, P. & Einav, I. 2012 Grainsize dynamics of polydisperse granular segregation down inclined planes. *J. Fluid Mech.* **690**, 499–511.

Ottino, J. M. & Khakhar, D. V. 2000 Mixing and segregation of granular materials. *Annu. Rev. Fluid Mech.* **32** (1), 55–91.

Ottino, J. M. & Lueptow, R. M. 2008 On mixing and demixing. *Science* **319** (5865), 912–913.

Powell, M. J. 1979 Site percolation in randomly packed spheres. *Phys. Rev. B* **20** (10), 4194.

Prasad, I., Santangelo, C. & Grason, G. 2017 Subjamming transition in binary sphere mixtures. *Phys. Rev. E* **96** (5), 052905.

Rousseau, H., Chassagne, R., Chauchat, J., Maurin, R. & Frey, P. 2021 Bridging the gap between particle-scale forces and continuum modelling of size segregation: application to bedload transport. *J. Fluid Mech.* **916**, A26.

Saitoh, K. & Tighe, B. P. 2019 Nonlocal effects in inhomogeneous flows of soft athermal disks. *Phys. Rev. Lett.* **122** (18), 188001.

Schlick, C. P., Fan, Y., Isner, A. B., Umbanhowar, P. B., Ottino, J. M. & Lueptow, R. M. 2015 Modeling segregation of bidisperse granular materials using physical control parameters in the quasi-2d bounded heap. *AIChE J.* **61** (5), 1524–1534.

Staron, L. 2018 Rising dynamics and lift effect in dense segregating granular flows. *Phys. Fluids* **30** (12), 123303.

Staron, L. & Phillips, J. C. 2014 Segregation time-scale in bi-disperse granular flows. *Phys. Fluids* **26** (3), 033302.

Staron, L. & Phillips, J. C. 2015 Stress partition and microstructure in size-segregating granular flows. *Phys. Rev. E* **92** (2), 022210.

Thornton, A. R. 2021 A brief review of (multi-scale) modelling approaches to segregation. *EPJ Web Conf.* **249**, 01004.

Trewhela, T., Ancey, C. & Gray, J. M. N. T. 2021 An experimental scaling law for particle-size segregation in dense granular flows. *J. Fluid Mech.* **916**, A55.

Tripathi, A. & Khakhar, D. V. 2011 Numerical simulation of the sedimentation of a sphere in a sheared granular fluid: a granular Stokes experiment. *Phys. Rev. Lett.* **107** (10), 108001.

Tripathi, A., Kumar, A., Nema, M. & Khakhar, D. V. 2021 Theory for size segregation in flowing granular mixtures based on computation of forces on a single large particle. *Phys. Res. E* **103** (3), L031301.

Tunuguntla, D. R., Bokhove, O. & Thornton, A. R. 2014 A mixture theory for size and density segregation in shallow granular free-surface flows. *J. Fluid Mech.* **749**, 99–112.

Tunuguntla, D. R., Weinhart, T. & Thornton, A. R. 2017 Comparing and contrasting size-based particle segregation models. *Comput. Part. Mech.* **4** (4), 387–405.

Umbanhowar, P. B., Lueptow, R. M. & Ottino, J. M. 2019 Modeling segregation in granular flows. *Annu. Rev. Chem. Biomol. Eng.* **10**, 129–153.

van der Vaart, K., Gajjar, P., Epely-Chauvin, G., Andreini, N., Gray, J. M. N. T. & Ancey, C. 2015 Underlying asymmetry within particle size segregation. *Phys. Rev. Lett.* **114** (23), 238001.

van der Vaart, K., van Schrojenstein Lantman, M. P., Weinhart, T., Luding, S., Ancey, C. & Thornton, A. R. 2018 Segregation of large particles in dense granular flows suggests a granular Saffman effect. *Phys. Rev. Fluids* **3** (7), 074303.

Ziff, R. M. & Torquato, S. 2017 Percolation of disordered jammed sphere packings. *J. Phys. A Math. Theor.* **50** (8), 085001.